HHS Public Access

Author manuscript

Cell Rep. Author manuscript; available in PMC 2021 August 24.

Published in final edited form as:

Cell Rep. 2021 August 17; 36(7): 109556. doi:10.1016/j.celrep.2021.109556.

Tubulin acetylation promotes penetrative capacity of cells undergoing radial intercalation

Caitlin Collins[1], **Sun K. Kim**[1], **Rosa Ventrella**[1], **Herve M. Carruzzo**[2], **Juliana C. Wortman**[2], **Hyebin Han**[1], **Evelyn E. Suva**[1], **Jennifer W. Mitchell**[1], **Clare C. Yu**[2], **Brian J. Mitchell**[1,3,*]

[1]Department of Cell and Developmental Biology, Lurie Comprehensive Cancer Center, Northwestern University, Feinberg School of Medicine, 303 E. Chicago Ave, Chicago, IL 60611, USA

[2]Department of Physics and Astronomy, University of California, Irvine, Irvine, CA 92697, USA

[3]Lead contact

SUMMARY

Post-translational modification of tubulin provides differential functions to microtubule networks. Here, we address the role of tubulin acetylation on the penetrative capacity of cells undergoing radial intercalation, which is the process by which cells move apically, insert between outer cells, and join an epithelium. There are opposing forces that regulate intercalation, namely, the restrictive forces of the epithelial barrier versus the penetrative forces of the intercalating cell. Positively and negatively modulating tubulin acetylation in intercalating cells alters the developmental timing such that cells with more acetylation penetrate faster. We find that intercalating cells preferentially penetrate higher-order vertices rather than the more prevalent tricellular vertices. Differential timing in the ability of cells to penetrate different vertices reveals that lower-order vertices represent more restrictive sites of insertion. We shift the accessibility of intercalating cells toward more restrictive junctions by increasing tubulin acetylation, and we provide a geometric-based mathematical model that describes our results.

Graphical Abstract

*Correspondence: brian-mitchell@northwestern.edu.

AUTHOR CONTRIBUTIONS

C.C., S.K.K., R.V., and B.J.M. conceived the experiments and wrote the manuscript. C.C., S.K.K., R.V., and J.W.M. performed the initial experiments and analysis. S.K.K., R.V., H.H.H., E.E.S., and J.W.M. performed experiments and analysis during revision. H.M.C., J.C.W., and C.C.Y. generated and wrote the mathematical model.

SUPPLEMENTAL INFORMATION

Supplemental information can be found online at https://doi.org/10.1016/j.celrep.2021.109556.

DECLARATION OF INTERESTS

The authors declare no competing interests.

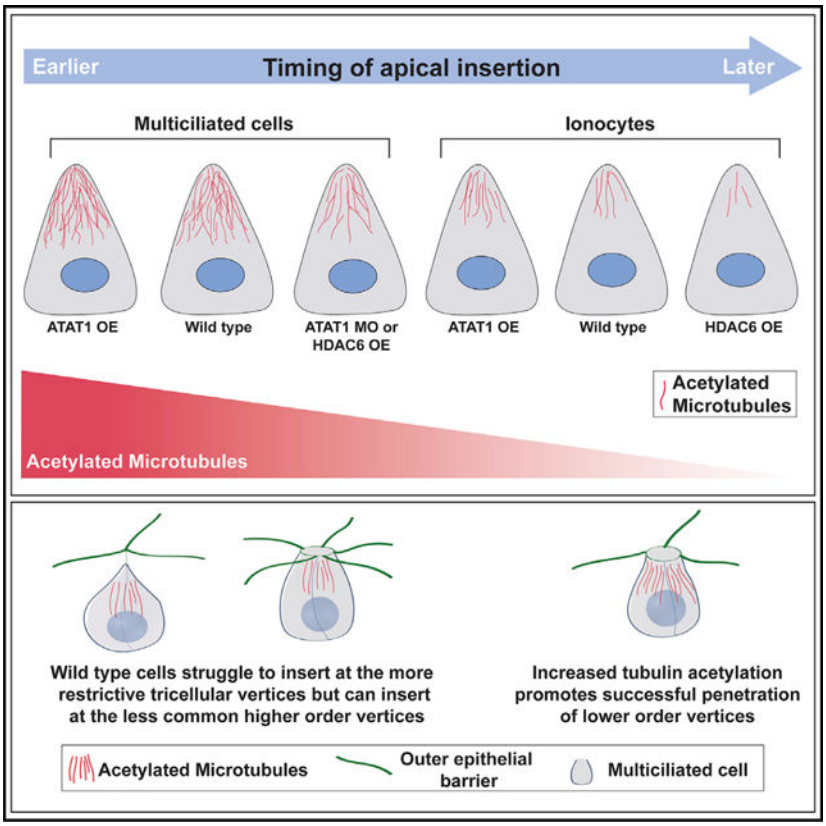

In brief

Collins et al. demonstrate the importance of tubulin acetylation during radial intercalation in *Xenopus* embryonic skin. Cells preferentially penetrate at less common higher-order vertices, requiring them to sample multiple vertices. Increasing acetylation allows penetration at the more common tricellular vertices that requires less sampling.

INTRODUCTION

Epithelia represent a barrier between different tissues or the external environment. Critical to this function, they must maintain epithelial integrity during a diverse array of insults including injury and disease. In contrast, the ability of cells to penetrate epithelial barriers is important for proper development and tissue homeostasis. The balance between maintaining epithelial integrity and allowing cell penetration is a complex interplay involving cell signaling, junctional remodeling, directed cell movements, and cytoskeletal dynamics. Here, we address the role of tubulin acetylation on both the timing and the vertex accessibility of cells undergoing radial intercalation into the epithelium of *Xenopus* embryonic skin.

During *Xenopus* development, both multiciliated cells (MCCs) and ionocytes (ICs) differentiate in a sublayer of the epithelium. To become functional, these cells must undergo a short apical migration and insert into the outer epithelium in a process called radial intercalation. Radial intercalation involves multiple steps requiring cells to (1) migrate in the apical direction, (2) penetrate the epithelial barrier by apically inserting between

outer epithelial cells, and (3) expanding their apical surface until they achieve proper size (Collins et al., 2020b). Cytoskeletal forces are known to be integral cell autonomous features of the intercalation process. Actin-based forces, as well as small GTPase activity, drive apical expansion of MCCs (Ioannou et al., 2013; Kim et al., 2012; Kulkarni et al., 2018; Sedzinski et al., 2016, 2017). Additionally, we have previously shown that centriole number and the subsequent changes to microtubule (MT) accumulation can regulate the timing of apical insertion, such that cells with more centrioles or more MTs insert earlier than cells with less (Collins et al., 2020a). Although these results clearly establish a critical role for MTs during intercalation, the functional mechanism of how MTs promote apical insertion remains poorly understood. Finally, the punctate pattern of MCC intercalation appears to be driven at least in part by S*cf*Kit-based repulsion of early pre-insertion motile MCCs that helps establish regular spacing (Chuyen et al., 2021).

MTs have numerous cellular functions, including providing the tracks for intracellular motor-based trafficking, facilitating the generation of cellular polarity, and providing the physical forces for diverse processes (e.g., mitosis). It is well established that MTs play critical roles during cellular migration including facilitating the transport of membrane-bound vesicles and signaling molecules to the leading edge (Etienne-Manneville, 2013). Most MT-based functions require MT directionality. We have previously reported that MTs are essential for regulating the timing of apical insertion during intercalation but importantly an increase in MTs in any orientation promotes insertion (Collins et al., 2020a). These results suggest that MTs may have a critical function independent of vesicle trafficking. Tubulin acetylation is known to promote the stabilization of MTs and lead to longer lived MTs that are more resistant to strain and more easily repaired (Janke and Montagnac, 2017; Xu et al., 2017). Additionally, acetylated MTs promote motor-based trafficking (Alper et al., 2014; Nekooki-Machida and Hagiwara, 2020; Reed et al., 2006). Furthermore, the acetylation of MTs has known roles in promoting cell migration and invasive behavior in numerous contexts, most notably in collective cell migration where it promotes focal adhesion stability (Bance et al., 2019; Boggs et al., 2015; Castro-Castro et al., 2012). Here, we test the hypothesis that acetylated MTs modulate both the timing of apical insertion and the penetration through more restrictive lower-order vertices.

Radial intercalation has been primarily addressed from the perspective of the intercalating cell, and yet the surrounding tissue environment likely contributes significantly to the process. Long-range cell migration events require chemo-attractant and chemo-repulsive signals (Szabó and Mayor, 2018). In fact, during *Xenopus* epiboly when cells radially intercalate to promote tissue thinning, cells respond to the chemo-attractant C3a (Szabó et al., 2016). However, there is no evidence to date that the short single-cell layer radial intercalation of MCCs and ICs into the skin requires external cues. Furthermore, tissue features such as substrate stiffness are known to contribute to collective cell movements in multiple contexts, including neural crest migration, but are unlikely to contribute significantly to the short individual cell movements of radial intercalation (Barriga et al., 2018; Barriga and Mayor, 2019; Szabó and Mayor, 2018; Zanotelli et al., 2019). Additionally, cellular arrangements provide a variety of tissue topologies that could offer differential access to intercalating cells. In the *Drosophila* oocyte, it has recently been shown that migrating border cells prefer a central path through the egg chamber that represents

the topographical path of least resistance via increased spacing between cells (Dai et al., 2020). In *Xenopus* skin, it has been reported that intercalating cells penetrate exclusively at multi-cellular vertices rather than between two cells (Stubbs et al., 2006). This information implies that vertices represent weak spots in the epithelium. Moreover, it is known that during the massive tissue remodeling that occurs during convergent-extension elongations that the sites of active movement are often associated with rosette vertices, sites where 5 or 6 cells come together (Blankenship et al., 2006; Lienkamp et al., 2012; Vanderleest et al., 2018). This predilection for higher-order vertices suggests that they represent more pliable sites of epithelial transformation. However, how the variability of vertex number affects the ability of cells to penetrate during radial intercalation remains unexplored. Here, we address the preference of MCCs for intercalating between higher-order vertices (e.g., rosettes) and the malleability of that preference toward the more restrictive lower-order tricellular vertices based on modulating the penetrative capacity of the intercalating cell.

RESULTS

MTs are important for the intercalation of both MCCs and ICs. Increasing centriole number results in an increase in MTs and precocious apical insertion (Collins et al., 2020a). In contrast, treatment with the MT depolymerizing drug nocodazole leads to partial intercalation for which cells do not achieve a normal apical size (Werner et al., 2014). Here, we have built on these results by performing an analysis of the timing of apical insertion in the presence of nocodazole. Radial intercalation is a progressive process, but we have previously defined the initial apical insertion event as the point at which cells achieve a small apical size of 35 μm^2, which is equivalent to the average size of the apical domain at the earliest stage observed (Collins et al., 2020a). Here, we show that cells treated with nocodazole are delayed specifically in apical insertion such that at each developmental stage (ST) significantly fewer MCCs or ICs had successfully penetrated the epithelial barrier (Figures S1A–S1D). Surprisingly, we have observed that most MTs found in intercalating cells are acetylated (Werner et al., 2014). In wild-type (WT) embryos, we found a natural variation in the amount of acetylated tubulin, and at ST20 when roughly 40% of MCCs have inserted, we found that cells with more acetylated tubulin were more likely to have inserted (Figures S1E and S1F) (Collins et al., 2020a). Acetylated MTs have been reported to be more stable, more flexible, and more resistant to strain, leading us to hypothesize that the acetylation of MTs provides added strength or flexibility to the MT network that facilitates their ability to penetrate through the epithelial barrier during apical insertion (Xu et al., 2017).

To test our hypothesis, we have exploited the use of the α-tubulin (Tub) promoter to mark and drive the expression of proteins specifically in MCCs and the pendrin (Pen) promoter to mark and drive the expression in a subset of ICs, as has been previously reported (Quigley et al., 2011; Stubbs et al., 2006). We first used the Tub promoter to drive overexpression (OE) of the deacetylase HDAC6 tagged with GFP (Tub-HDAC6-GFP) in post-mitotic MCCs prior to radial intercalation (Stubbs et al., 2006). We did not see a significant difference in the overall MT network as quantified by the fluorescent intensity of antibody staining by using a beta-tubulin antibody (Figures 1A and 1C). In contrast, we did observe a significant decrease in tubulin acetylation by acetylated tubulin antibody staining in MCCs with an

OE of HDAC6 (Figures 1B and 1D). Importantly, when we performed a time course of MCC intercalation, we found that there was a significant delay in apical insertion with fewer cells having successfully penetrated the outer epithelium at each time point (Figures 1E and 1F). Ultimately, the typical number of MCCs intercalate, but the delay in apical insertion suggests that tubulin acetylation and the corresponding change in the MT network are important for providing the protrusive ability required for MCCs to quickly penetrate the outer epithelium. HDAC6 has numerous cellular targets; so to more rigorously test the importance of tubulin acetylation in MCCs, we have generated a morpholino oligo (MO; Gene Tools, LLC) to the main tubulin acetylating enzyme alpha-tubulin N-acetyltransferase (ATAT1). In MCCs containing the ATAT1 MO, there is a decrease in both overall MTs and acetylated MTs, which is rescued by the addition of GFP-ATAT1 not targeted by the MO (Figures S2A–S2D). Using the transgenic *Xenopus* line Xla.Tg(Tuba1a:MyrPalm-mRFP1)^{NXR} that we, here, called Tub-mRFP, we generated mosaic embryos and found that at ST22 most MCCs had apically inserted with or without a control MO. In contrast, in embryos mosaic for ATAT1 MO, the non-MO cells had mostly inserted, whereas the MO cells had mostly failed (Figures S2E–S2H). Importantly, the failure to insert was partially rescued by the addition of GFP-ATAT1. The results at multiple time points suggests that ATAT1 MO causes a delay but ultimately not a block in apical insertion similar to HDAC6 (Figure 1F).

ICs have considerably fewer MTs than MCCs and are slower in their progression through radial intercalation, with the primary delay being in apical insertion. We have shown that expression of the MT (−) end protein CAMSAP1 fused to the apically positioned Par6 protein (CAMSAP1-Par6) increases MTs in ICs and is sufficient to drive precocious apical insertion (Collins et al., 2020a). Here, we have addressed whether the acetylation status of these ectopic MTs is important for driving this precocious insertion. As previously reported, injection of the CAMSAP1-Par6 fusion protein leads to a substantial amount of apically positioned MTs (Figure 1G). Importantly, co-injection with HDAC6 significantly lowered the fluorescent intensity of acetylated MTs but not the overall amount of MTs (Figures 1G–1J). In addition, the precocious apical insertion observed with CAM-SAP1-Par6 is abrogated by the addition of HDAC6 and insertion rates revert to WT levels (Figures 1K and 1L; Figure S3A; Collins et al., 2020a). This finding suggests that MTs in general are not sufficient to promote intercalation but that those MTs must be acetylated.

To further test the effect of acetylated MTs in promoting apical insertion, we induced an OE of ATAT1 to increase MT acetylation in intercalating cells. Tub-ATAT1 expressed specifically in MCCs results in a slight increase in acetylation and a modest but significant increase in cells that apically insert at ST18, with this trend continuing at ST20 and ST22 (Figures 2A–2F; Figure S3B). Although the ATAT1 OE result is consistent with our hypothesis that acetylation is important for apical insertion, the already high levels of acetylation in MCCs likely limit the effectiveness. Consistent with this result, we see a stronger effect on the apical insertion of ICs when we induced an OE of ATAT1. Pen-ATAT1 OE in ICs resulted in a significant and robust increase in tubulin acetylation and a stronger, significant increase in cells that intercalate at ST20 and ST22 (Figures 2G–2L). These results further implicate MT acetylation in promoting apical insertion. We interpret these

results to indicate that cells with increased tubulin acetylation have an increased penetrative capacity during radial intercalation.

The process of radial intercalation represents a complex interplay between the intercalating cells and the surrounding outer epithelial tissue. In particular, it has been previously reported that cells intercalate exclusively at multicellular vertices rather than between two cells (Stubbs et al., 2006). One interpretation of this observation is that vertices represent weak points in the epithelial barrier that are more easily penetrated. Interestingly, in the complex epithelium of *Xenopus* skin, there is a variety of different types of vertices ranging from tricellular junctions to rosettes with 5 or 6 cells (Figure 3A). We hypothesized that different types of vertices would provide differential barrier strengths against the penetration of intercalating cells. We performed a live-imaging analysis of vertex preference during the early phases of MCC intercalation (ST17–ST20). We focused on MCCs specifically because the epithelium is relatively stable during these early stages and MCCs almost never intercalate next to one another, which would complicate the interpretation of vertex strength. In contrast, a similar analysis of ICs is not feasible due to the changing vertex environment caused primarily by the intercalation events of the MCCs coupled with the fact that ICs often intercalate adjacent to the sites of MCC intercalation (Drysdale and Elinson, 1992; Dubaissi and Papalopulu, 2011; Stubbs et al., 2006), likely due to the weakened epithelium caused by MCC intercalation.

From our live-imaging videos (e.g., Video S1) we scored the overall number of each type of vertex and found that tricellular vertices were the most common, making up 59% of all vertices (Figures 3A and 3B). Four-cell vertices represented 33%, and 5- or 6-cell vertices, called rosettes, accounted for 5% and 2% of vertices, respectively (Figure 3B). Interestingly, despite the large number of tricellular vertices, we found that MCCs rarely apically inserted at these sites during our live-imaging experiments, representing only 6% of insertion events (Figure 3B). Four-cell vertices, despite being less frequent then tricellular vertices, accounted for close to 60% of all intercalation events (Figure 3B). Finally, although rosettes are rare, they account for 34% of intercalation events, clearly showing that MCCs have a preference for higher-order vertices. In fact, of all 5- and 6-cell vertices, nearly 100% are sites of MCC intercalation between ST17 and ST20 (Figure 3C). In contrast, approximately 42% of all 4-cell vertices and only 3% of all tricellular vertices are sites of successful apical insertion during this period of MCC intercalation (Figure 3C). Interestingly, when the timing of intercalation at each type of vertex is analyzed, a clear pattern arises in which cells intercalate earlier at higher-order vertices. We scored the cumulative number of cells that intercalate at each type of vertex throughout our time lapse and then quantified the time when 50% of those cells had successfully breached the epithelium (T_{50}; indicated by the dotted red line in Figures 4A–4D). We found that for 6-cell vertices, the T_{50} for MCCs that would eventually occupy a 6-cell vertex was approximately 30 min. The T_{50} of 5-cell vertices was slightly slower (~70 min), suggesting that these vertices are harder to penetrate. This trend continues, with 4-cell vertices having a T_{50} of ~100 min and tricellular vertices having a T_{50} of ~160 min. The striking regularity of these temporal differences suggests that the challenges of penetrating each type of vertices increases as vertex cell number decreases. Also, our T_{50} quantification suggested a variable strength to the epithelial barrier, and we

were curious if we could exploit these differences to test the malleability of the penetrative capacity for intercalating cells.

Knowing the relative timing of apical insertion for each vertex type gives us a powerful assay with which to address the relative contribution of tubulin acetylation to the penetrative strength of intercalating MCCs. When analyzing fixed tissues at ST20, we found that only 11% of all MCC intercalation events occurred at tricellular vertices (Figure 4E). We hypothesized that if this low percentage was due to the restrictive strength of the tricellular barrier, then this number would be malleable if we altered the penetrative capacity of the intercalating cell by modulating MT number and acetylation. To test this hypothesis, we first reduced the penetrative capacity by injecting embryos with Tub-HDAC6 to lower MT acetylation, and we consistently found that now fewer cells (8%) were able to successfully insert by ST20 (Figure 4E). We next induced an OE the MT nucleating factor XMAP215. Although we found a slight increase in overall MTs, we found a significant increase in acetylated MTs (Figures S4A–S4D). Importantly, this increase lead to a significant increase in the number of MCCs that successfully inserted at tricellular junctions by ST20 (15%; Figure 4E). Increasing MT acetylation by OE of ATAT1 had an even stronger effect, increasing penetration to 20% (Figure 4E). Importantly, OE of both XMap215 and ATAT1 led to an additive increase (23%) of MCCs that were able to apically insert by ST20. These results indicate that increasing the number of acetylated MTs leads to an increased penetrative capacity, allowing cells to infiltrate between the restrictive tricellular junctions at a stage (ST20) when most WT cells fail.

Next, we generated a geometric model for the preference of MCCs to insert at each vertex type. Although MCCs are capable of some lateral motion (Chuyen et al., 2021), the initial assumption of this model is that MCCs have a limited number of vertices in their neighborhood that are potential sites of insertion. We define that number as q. We also note that MCCs often simultaneously overlap with several (2–4) vertices (e.g., Video S2). We further assume higher-order vertices are easier to insert than lower-order vertices. Thus, of the q vertices sampled, an MCC will insert into the vertex with the largest number of edges (cells). There are 4 types of vertices defined by the number of edges ranging from 3 to 6. Each occurs with probability p_k with $k = 3,4,5,6$. The problem thus reduces to finding the probability of a neighborhood where a particular k-vertex exists and no larger vertices occur. Then, the MCC will go through the k-vertex. This probability, $P_q(k)$, is easy to derive (see Equation 2 in Figure S4E):

$$P_q(k) = \left(1 - \sum_{k' > k}^{6} p_{k'}\right)^q - \left(1 - \sum_{k' \geq k}^{6} p_{k'}\right)^q \quad \text{(Equation 1)}$$

This is the probability that an MCC will come through a k-vertex. Using a range of values for the number of vertices that an MCC will explore (q), we show the values of $P_q(k)$ computed with Equation 1 in Figure 4H.

The predictions of the fraction of MCCs that insert at each vertex type are most closely aligned with the experimental data using a q value of 5 or 6. Given that cells likely sample variable numbers of vertices, we sought to determine the experimental value for q by using

long-term imaging of Tub-GFP-labeled MCCs prior to apical insertion (~ST14–ST18). We scored the number of unique vertices that an MCC comes into contact with and found that on average a cell interacts with 5.5 vertices (median of 5; Figure 4F; Video S2). Interestingly, we found that in MCCs in which we induced an OE of ATAT1, cells sampled on average only 3.7 vertices (median 3; Figure 4F; Video S3). Figure 4H presents a table showing a hypothetical shift of tricellular insertions increasing from 7.8% to 21.3% when the q value is changed from 5 to 3. Interestingly, our ST20 analysis of tricellular insertion showed a similar shift from 10% to 20% (Figure 4E). This result indicates that our observed shift in the preference of MCCs to insert at tricellular junctions in ATAT1 OE cells is reflected in the shift in q and that ATAT1 cells choose a suitable vertex with less sampling (Figure 4F), which is also consistent with the observed precocious apical insertion (Figures 2E and 2F). Importantly, we found that control and ATAT1 cells sampled vertices at the same rate (0.032 and 0.030 vertices per min), indicating a shift in preference that allows insertion at lower-order vertices in ATAT1 OE cells. Although our model nicely predicts that cells that intercalate at more restrictive lower-order vertices (e.g., ATAT1 OE) sample fewer vertices, it does not explain why MCCs normally prefer higher-order vertices. Furthermore, although our data clearly show that cells with more acetylated tubulin can penetrate lower-order vertices, it remains unclear how these cells select a particular vertex. We propose that MCCs are constantly attempting to penetrate each vertex that they encounter and that cells with more acetylated tubulin simply succeed with fewer attempts due to an increase in penetrative capacity afforded by more stable and rigid MTs.

DISCUSSION

MTs are well-known modulators of cell migration and can facilitate the directional movement of membrane vesicles and signaling molecules to the leading edge. Acetylated MTs are more stable and more resistant to strain, offering the possibility that they can provide important structural features that deliver strength and rigidity to cells migrating in a 3D tissue environment. Additionally, the increased flexibility of acetylated MTs could further promote the penetration through cell junctions. Our data provide two important pieces of information that indicate a structural role for MTs in the tissue penetration of radial intercalation. First, in ICs with ectopic apically generated MTs (e.g., CAMSAP1-Par6; Figures 1G–1L), the precocious apical insertion is abrogated by the loss of acetylation, indicating that the presence of ectopic MTs alone is not sufficient to promote IC apical insertion, but that those MTs must be acetylated. Second, the penetration of MCCs at tricellular junctions is promoted separately and additively by the changes to MTs and MT acetylation. These results indicate that during MCC intercalation the enrichment of MTs is important and the acetylation of those MTs is also critical. Overall, we propose that MT acetylation facilitates radial intercalation by increasing penetrative capacity by increasing the strength and rigidity of the MT network.

Epithelial tissues provide a barrier function against liquids and toxins, as well as infectious agents. They also provide a barrier to cells attempting to penetrate. Recently, it has been proposed that the topological environment of multiple cells coming together offers an easier passage for groups of cells undergoing migration through the *Drosophila* egg chamber (Dai et al., 2020). Our results extend these observations by indicating that this preference for

migrating between higher-order vertices is a widespread evolutionarily conserved feature of diverse tissues with distinct modes of tissue penetration. In addition to bulk collective cell movements, individual cells undergoing radial intercalation also prefer to penetrate at the sites of higher-order vertices. More importantly, our results in MCCs indicate that this preference is malleable based on the penetrative capacity of the migrating cell. Consistent with our results, ICs intercalate after MCCs, in part due to lower numbers of centrioles and MTs that would result in a lower penetrative capacity. Interestingly, in *Xenopus* embryos, it has been reported that OE of the constitutively active Notch intracellular domain (NICD) leads to a dramatic loss in MCCs but does not affect IC fate (Stubbs et al., 2006). In the absence of MCCs, there is a significant delay in IC intercalation. This result suggests that the ICs have a weaker penetrative capacity and that they rely on MCC intercalation to create more higher-order vertices to facilitate their intercalation. Consistent with this idea, ICs typically intercalate adjacent to MCCs (Stubbs et al., 2006).

There is an ongoing balance between the restrictive competence of the epithelium and the invasive capacity of penetrating cells (Figure 4G). This balance is complex and uses the regulation of junctional remodeling and diverse cytoskeletal elements. Here, we provide evidence that one cytoskeletal feature, namely, the acetylation of MTs specifically in intercalating cells, increases the ability of cells to penetrate by both increasing the overall rate of apical insertion and by facilitating the penetration at more restrictive lower-order tricellular vertices.

STAR★METHODS

RESOURCE AVAILABILITY

Lead contact—Further information and requests for resources and reagents should be directed to and will be fulfilled by the lead contact, Brian Mitchell (brian-mitchell@northwestern.edu).

Materials availability—All unique reagents and biological material generated in this study are available from the lead contact, Brian Mitchell.

Data and code availability—This study did not generate any unique datasets or code. Any additional information required to reanalyze the data reported in this paper is available from the lead contact upon request.

EXPERIMENTAL MODEL AND SUBJECT DETAILS

Xenopus laevis were used and maintained in accordance with standards established by the Northwestern University Institutional Animal Care and Use Committee (IS00001612). Mature *X. laevis* frogs were obtained from NASCO (Fort Atkinson, WI). Frogs were housed in a recirculating tank system with regularly monitored temperature and water quality (pH, conductivity, and nitrate/nitrite levels) at a temperature of 16–18°C and were fed frog brittle. For live imaging and nocodazole experiments, embryos from Tub-Deup1-GFP and Tub-mRFP transgenic lines (Xla.Tg(tuba1a:deup1-eGFP)^{NXR} and Xla.Tg(tuba1a:MyrPalm-mRFP1)^{NXR}) were generated and purchased from National

Xenopus Resource RRID:SCR_013731 at the Marine Biological Laboratory and were used to identify MCCs.

METHOD DETAILS

Embryo injections—All *Xenopus* experiments were performed using previously described techniques (Werner and Mitchell, 2013). In brief, *Xenopus* embryos were obtained by *in vitro* fertilization using standard protocols (Sive et al., 2007) approved by the Northwestern University Institutional Animal Care and Use Committee. Embryos were injected at the two- or four-cell stage with 40–250 pg mRNA or 10–20 pg of plasmid DNA. For all DNA injections (except for fixed vertices analysis, Figures 3 and 4), embryos were injected mosaically at the 2 or 4 cell stage such that only half of the embryo expressed the construct to avoid toxicity. For fixed MCC vertices analysis (Figures 3 and 4), embryos were injected 3 times in each blastomere at the 2 cell stage for maximal expression of the construct in as many MCCs as possible. Embryos were utilized at experimental STs as described through the paper between ST 17–28, prior to the sexual differentiation.

Plasmids/mRNA/morpholino—pCS2+ plasmids containing an N-terminal GFP or RFP as a tracer containing the α-tubulin promoter (TUBA1A-B on Scaffold 127187, pCS2tub) (Stubbs et al., 2006) were used to drive expression of some constructs specifically in MCCs. pCS2+ plasmids containing the Pendrin (Pen) promoter (Quigley et al., 2011) with an N-terminal GFP or RFP were used to drive expression of some constructs specifically in ICs (Collins et al., 2020a). The GFP-tricellulin construct was described previously, and the GFP-CAMSAP1-Par6 construct has been previously reported (Collins et al., 2020a). HDAC6-FLAG (#13823) and pEF5B-FRT-GFP-aTAT1 (#27099) were purchased from Addgene. Tub-GFP-HDAC6 was made by PCR amplifying the HDAC6 sequence from the HDAC6-FLAG construct and ligating the PCR amplicon into the Tub-GFP construct. MCC- and IC-specific ATAT1 constructs were made by PCR amplifying the ATAT1 sequences and ligating the PCR amplicons into Tub-RFP or Pen-RFP constructs, respectively. An XMAP215-WT-7His-GFP construct was a kind gift from Jay Gatlin and was previously described (Milunovic-Jevtic et al., 2018; Reber et al., 2013). Tub-XMAP215-GFP was made by PCR amplifying the xmap215 sequence and ligating the PCR amplicon into the Tub-XLT vector. mRNA was generated using the Sp6 *in vitro* mRNA transcription kit (Ambion) following linearization of plasmid DNA with NotI. Capped mRNA was isolated using an RNA isolation kit (QIAGEN). Morpholino antisense oligonucleotides (GeneTools) were used to inhibit the expression of *Xenopus* ATAT1. ATAT1 atg MO: 5′-GTGTACGTCAAACTCAAACTCCATG-3′ and a Control MO: 5′-CCTCTTACCTCAGTTACAATTTATA-3′ were used. Morpholinos were injected into one blastomere at the four-cell stage with membrane GFP as a tracer. Rescue experiments were performed by coinjecting GFP-ATAT1 mRNA.

Inhibitors—Nocodazole (Sigma, #M1404) was used to inhibit MT dynamics. Nocodazole treatments were performed between stages 13 and 28. In brief, embryos were incubated in the presence of 0.2 μM or 1 μM Nocodazole (in DMSO) or pure DMSO (vehicle) from ST13 until embryos were at the desired stage. Embryos were fixed in 3% PFA immediately thereafter.

Immunofluorescence—For antibody staining, embryos were fixed with 3% PFA in PBS, blocked in 10% goat serum, and primary and secondary antibody solutions were prepared in 5% goat serum. Mouse anti-acetylated α-tubulin (T7451; Sigma-Aldrich) was used at a 1:500 dilution, mouse anti-beta tubulin (DHSB; E7) supernatant was used at a 1:10 dilution. Mouse anti-FLAG M2 (F3165; Sigma) and rabbit anti-DYKDDDDK (2368; Cell Signaling) were used at 1:100 dilutions. E7 (anti-tubulin) was deposited to the DSHB by Klymkowsky, M (Chu and Klymkowsky, 1989). Cy-2–, Cy-3–, or Cy-5–conjugated goat anti-mouse secondary antibodies were used at the manufacturers' recommended dilution. Phalloidin 650 (1:600, Invitrogen) and Alexa Fluor Plus 405 Phalloidin (1:100, Invitrogen) were used to visualize actin. Embryos were mounted between two coverslips using Fluoro-Gel (Electron Microscopy Sciences).

Microscopy—All microscopy was performed on a laser-scanning confocal microscope (A1R; Nikon) using a 20 × water objective lens (live imaging) or a 60 × oil Plan-Apochromat objective lens with a 1.4 NA (fixed imaging). Nikon Elements Software was used for all acquisition and image processing. For all fixed images, multiple z planes were visualized in 0.4 μm steps (4–10 μm total depth). For live imaging, a 20 μm range was imaged with 0.5 μm steps. Images were acquired every 10 minutes for the duration of the time lapse. Images are maximum intensity projections of z stacks. Images were processed in Nikon Elements Software.

QUANTIFICATION AND STATISTICAL ANALYSIS

Tubulin intensity analysis—For acetylated and beta tubulin intensity measurements, a z-projection of the intercalating cell was created and the fluorescence intensity was measured in ImageJ by outlining the cell of interest and measuring anti-acetylated or anti-beta tubulin fluorescence within the outline. Tubulin intensities were normalized relative to the mean fluorescence intensity measured in 'control' (uninjected cells) in mosaic embryos for each experiment.

Apical insertion analysis—Apical area of intercalating cells was measured at each stage (based on phalloidin staining). For apical insertion analysis, an apical domain area of 35 μm^2 was set as a threshold to determine apical insertion based analysis previously described (Collins et al., 2020a). The percentage of MCCs or ICs apically inserted (as opposed to still below the surface) at each stage represent the percentage of cells measured at the indicated stage that have an area > 35 μm^2 and is independent of measurements taken at other stages. For all apical insertion analyses, cells below the surface of the outer epithelium were included in the analysis and were given an apical area of 0 μm^2.

Live imaging and MCC vertices analysis—For live imaging analysis, the composition of vertices prior to intercalation was determined by counting the total number of each type of vertex present in the first frame of the time lapse (Figure 4). To determine the percentages of where MCCs intercalate (Figures 3 and 4), all MCCs that breached the outer epithelium were analyzed for the type of vertex where they inserted. Vertex occupancy was calculated for each type of vertex by dividing the number of vertices that were a site of MCC intercalation by the end of the time lapse by the total number of each type

of vertex counted at the beginning of the time lapse. Bar graphs showing cumulative progression of MCC intercalation at 3, 4, 5, and 6 cell vertices were generated by counting the total number of MCCs that intercalated at each vertex type during the entire time lapse. Cumulative progression of MCC intercalation was calculated at each time point by dividing the cumulative number of MCCs that had inserted at the vertex of interest by the total number of all MCCs that intercalated at that vertex type by the end of the time lapse. The red dotted line on the bar graph represents the time at which 50% of all MCCs that would intercalate at the vertex type had already breached the outer epithelium. Bar graphs displaying cumulative progression of MCC intercalation at different vertex types are representative of data collected for 214 MCCs in one experiment. Similar trends in timing of intercalation 3, 4, 5, and 6 cell vertices were observed in other time lapse experiments. For fixed vertices analyses, embryos fixed at stage 20 were analyzed for sites of MCC intercalation by counting the number of all MCCs expressing the construct of interest that had established an apical domain. The percentage of cells that had intercalated as tricellular vertices was calculated by dividing the number of MCCs expressing each construct that had intercalated at tricellular vertices by the total number of MCCs expressing the construct of interest that had established an apical domain. The data in Figure 4F was collected from either Control or ATAT1 OE embryos containing tub-GFP to mark MCCs and were imaged at 20X for 4 Hrs (stack every 10 minutes). We then quantified how many unique vertices each MCC touched from the time we first see them until they apically insert.

Image presentation and statistical analysis—Some images were smoothed and processed for figure presentation only. Raw images were used for all analyses. Significance was determined with a Student's t test (Figures 1C, 1D, 1I, 1J, 2C, 2D, 2I, 2J, 4E, and S2D) and Chi-square test for (Figures 1F, 1L, 2F, 2L, S1C, and S1D). For all bar graphs, bars represent the mean and error bars indicate the standard deviation (SD). Statistical information including experimental numbers can be found in the figure legends whereas p values can be found in the figures. For all statistical analyses, $*p < 0.05$, $**p < 0.01$, and $***p < 0.001$.

Supplementary Material

Refer to Web version on PubMed Central for supplementary material.

ACKNOWLEDGMENTS

This work was supported by NIH/NIGMS to B.J.M. (R01GM119322). R.V. was supported from the Cutaneous Biology training grant (TGM32AR060710). We would like to thank the National *Xenopus* Resource and the Marine Biological Laboratories for technical support and reagents.

REFERENCES

Alper JD, Decker F, Agana B, and Howard J (2014). The motility of axonemal dynein is regulated by the tubulin code. Biophys. J 107, 2872–2880. [PubMed: 25658008]

Bance B, Seetharaman S, Leduc C, Boëda B, and Etienne-Manneville S (2019). Microtubule acetylation but not detyrosination promotes focal adhesion dynamics and astrocyte migration. J. Cell Sci 132, jcs225805. [PubMed: 30858195]

Barriga EH, and Mayor R (2019). Adjustable viscoelasticity allows for efficient collective cell migration. Semin. Cell Dev. Biol 93, 55–68. [PubMed: 29859995]

Barriga EH, Franze K, Charras G, and Mayor R (2018). Tissue stiffening coordinates morphogenesis by triggering collective cell migration in vivo. Nature 554, 523–527. [PubMed: 29443958]

Blankenship JT, Backovic ST, Sanny JS, Weitz O, and Zallen JA (2006). Multicellular rosette formation links planar cell polarity to tissue morphogenesis. Dev. Cell 11, 459–470. [PubMed: 17011486]

Boggs AE, Vitolo MI, Whipple RA, Charpentier MS, Goloubeva OG, Ioffe OB, Tuttle KC, Slovic J, Lu Y, Mills GB, and Martin SS (2015). α-Tubulin acetylation elevated in metastatic and basal-like breast cancer cells promotes microtentacle formation, adhesion, and invasive migration. Cancer Res. 75, 203–215. [PubMed: 25503560]

Castro-Castro A, Janke C, Montagnac G, Paul-Gilloteaux P, and Chavrier P (2012). ATAT1/MEC-17 acetyltransferase and HDAC6 deacetylase control a balance of acetylation of alpha-tubulin and cortactin and regulate MT1-MMP trafficking and breast tumor cell invasion. Eur. J. Cell Biol 91, 950–960. [PubMed: 22902175]

Chu DT, and Klymkowsky MW (1989). The appearance of acetylated alpha-tubulin during early development and cellular differentiation in Xenopus. Dev. Biol 136, 104–117. [PubMed: 2680681]

Chuyen A, Rulquin C, Daian F, Thomé V, Clément R, Kodjabachian L, and Pasini A (2021). The Scf/Kit pathway implements self-organized epithelial patterning. Dev. Cell 56, 795–810.e7. [PubMed: 33756121]

Collins C, Majekodunmi A, and Mitchell B (2020a). Centriole Number and the Accumulation of Microtubules Modulate the Timing of Apical Insertion during Radial Intercalation. Curr. Biol 30, 1958–1964.e1953. [PubMed: 32243862]

Collins C, Ventrella R, and Mitchell BJ (2020b). Building a ciliated epithelium: Transcriptional regulation and radial intercalation of multiciliated cells. In Current Topics in Developmental Biology, Sokol S, ed. (Academic Press).

Dai W, Guo X, Cao Y, Mondo JA, Campanale JP, Montell BJ, Burrous H, Streichan S, Gov N, Rappel WJ, and Montell DJ (2020). Tissue topography steers migrating *Drosophila* border cells. Science 370, 987–990. [PubMed: 33214282]

Drysdale TA, and Elinson RP (1992). Cell Migration and Induction in the Development of the Surface Ectodermal Pattern of the Xenopus laevis Tadpole. Dev. Growth Differ 34, 51–59.

Dubaissi E, and Papalopulu N (2011). Embryonic frog epidermis: a model for the study of cell-cell interactions in the development of mucociliary disease. Dis. Model. Mech 4, 179–192. [PubMed: 21183475]

Etienne-Manneville S (2013). Microtubules in cell migration. Annu. Rev. Cell Dev. Biol 29, 471–499. [PubMed: 23875648]

Ioannou A, Santama N, and Skourides PA (2013). Xenopus laevis nucleotide binding protein 1 (xNubp1) is important for convergent extension movements and controls ciliogenesis via regulation of the actin cytoskeleton. Dev. Biol 380, 243–258. [PubMed: 23685253]

Janke C, and Montagnac G (2017). Causes and Consequences of Microtubule Acetylation. Curr. Biol 27, R1287–R1292. [PubMed: 29207274]

Kim K, Lake BB, Haremaki T, Weinstein DC, and Sokol SY (2012). Rab11 regulates planar polarity and migratory behavior of multiciliated cells in Xenopus embryonic epidermis. Dev. Dyn 241, 1385–1395. [PubMed: 22778024]

Kulkarni SS, Griffin JN, Date PP, Liem KF Jr., and Khokha MK (2018). WDR5 Stabilizes Actin Architecture to Promote Multiciliated Cell Formation. Dev. Cell 46, 595–610.e3. [PubMed: 30205038]

Lienkamp SS, Liu K, Karner CM, Carroll TJ, Ronneberger O, Wallingford JB, and Walz G (2012). Vertebrate kidney tubules elongate using a planar cell polarity-dependent, rosette-based mechanism of convergent extension. Nat. Genet 44, 1382–1387. [PubMed: 23143599]

Milunovic-Jevtic A, Jevtic P, Levy DL, and Gatlin JC (2018). In vivo mitotic spindle scaling can be modulated by changing the levels of a single protein: the microtubule polymerase XMAP215. Mol. Biol. Cell 29, 1311–1317. [PubMed: 29851557]

Nekooki-Machida Y, and Hagiwara H (2020). Role of tubulin acetylation in cellular functions and diseases. Med. Mol. Morphol 53, 191–197. [PubMed: 32632910]

Quigley IK, Stubbs JL, and Kintner C (2011). Specification of ion transport cells in the Xenopus larval skin. Development 138, 705–714. [PubMed: 21266406]

Reber SB, Baumgart J, Widlund PO, Pozniakovsky A, Howard J, Hyman AA, and Jülicher F (2013). XMAP215 activity sets spindle length by controlling the total mass of spindle microtubules. Nat. Cell Biol 15, 1116–1122. [PubMed: 23974040]

Reed NA, Cai D, Blasius TL, Jih GT, Meyhofer E, Gaertig J, and Verhey KJ (2006). Microtubule acetylation promotes kinesin-1 binding and transport. Curr. Biol 16, 2166–2172. [PubMed: 17084703]

Schneider CA, Rasband WS, and Eliceiri KW (2012). NIH Image to ImageJ: 25 years of image analysis. Nat. Methods 9, 671–675. [PubMed: 22930834]

Sedzinski J, Hannezo E, Tu F, Biro M, and Wallingford JB (2016). Emergence of an Apical Epithelial Cell Surface In Vivo. Dev. Cell 36, 24–35. [PubMed: 26766441]

Sedzinski J, Hannezo E, Tu F, Biro M, and Wallingford JB (2017). RhoA regulates actin network dynamics during apical surface emergence in multiciliated epithelial cells. J. Cell Sci 130, 420–428. [PubMed: 28089989]

Sive HL, Grainger RM, and Harland RM (2007). Xenopus laevis In Vitro Fertilization and Natural Mating Methods. CSH Protoc. 2007, pdb.prot4737.

Stubbs JL, Davidson L, Keller R, and Kintner C (2006). Radial intercalation of ciliated cells during Xenopus skin development. Development 133, 2507–2515. [PubMed: 16728476]

Szabó A, and Mayor R (2018). Mechanisms of Neural Crest Migration. Annu. Rev. Genet 52, 43–63. [PubMed: 30476447]

Szabó A, Cobo I, Omara S, McLachlan S, Keller R, and Mayor R (2016). The Molecular Basis of Radial Intercalation during Tissue Spreading in Early Development. Dev. Cell 37, 213–225. [PubMed: 27165554]

Vanderleest TE, Smits CM, Xie Y, Jewett CE, Blankenship JT, and Loerke D (2018). Vertex sliding drives intercalation by radial coupling of adhesion and actomyosin networks during *Drosophila* germband extension. eLife 7, e34586. [PubMed: 29985789]

Werner ME, and Mitchell BJ (2013). Using Xenopus Skin to Study Cilia Development and Function. In Methods in Enzymology, Volume 525: Cilia, Part B, Marshall WF, ed. (Academic Press).

Werner ME, Mitchell JW, Putzbach W, Bacon E, Kim SK, and Mitchell BJ (2014). Radial intercalation is regulated by the Par complex and the microtubule-stabilizing protein CLAMP/Spef1. J. Cell Biol 206, 367–376. [PubMed: 25070955]

Xu Z, Schaedel L, Portran D, Aguilar A, Gaillard J, Marinkovich MP, Théry M, and Nachury MV (2017). Microtubules acquire resistance from mechanical breakage through intralumenal acetylation. Science 356, 328–332. [PubMed: 28428427]

Zanotelli MR, Rahman-Zaman A, VanderBurgh JA, Taufalele PV, Jain A, Erickson D, Bordeleau F, and Reinhart-King CA (2019). Energetic costs regulated by cell mechanics and confinement are predictive of migration path during decision-making. Nat. Commun 10, 4185. [PubMed: 31519914]

Highlights

- Cells with more acetylated tubulin are more efficient at radial intercalation
- Tubulin acetylation modulates the rate of tissue penetration
- Multiciliated cells preferentially penetrate higher-order vertices
- Increasing acetylation promotes penetration at more restrictive tricellular vertices

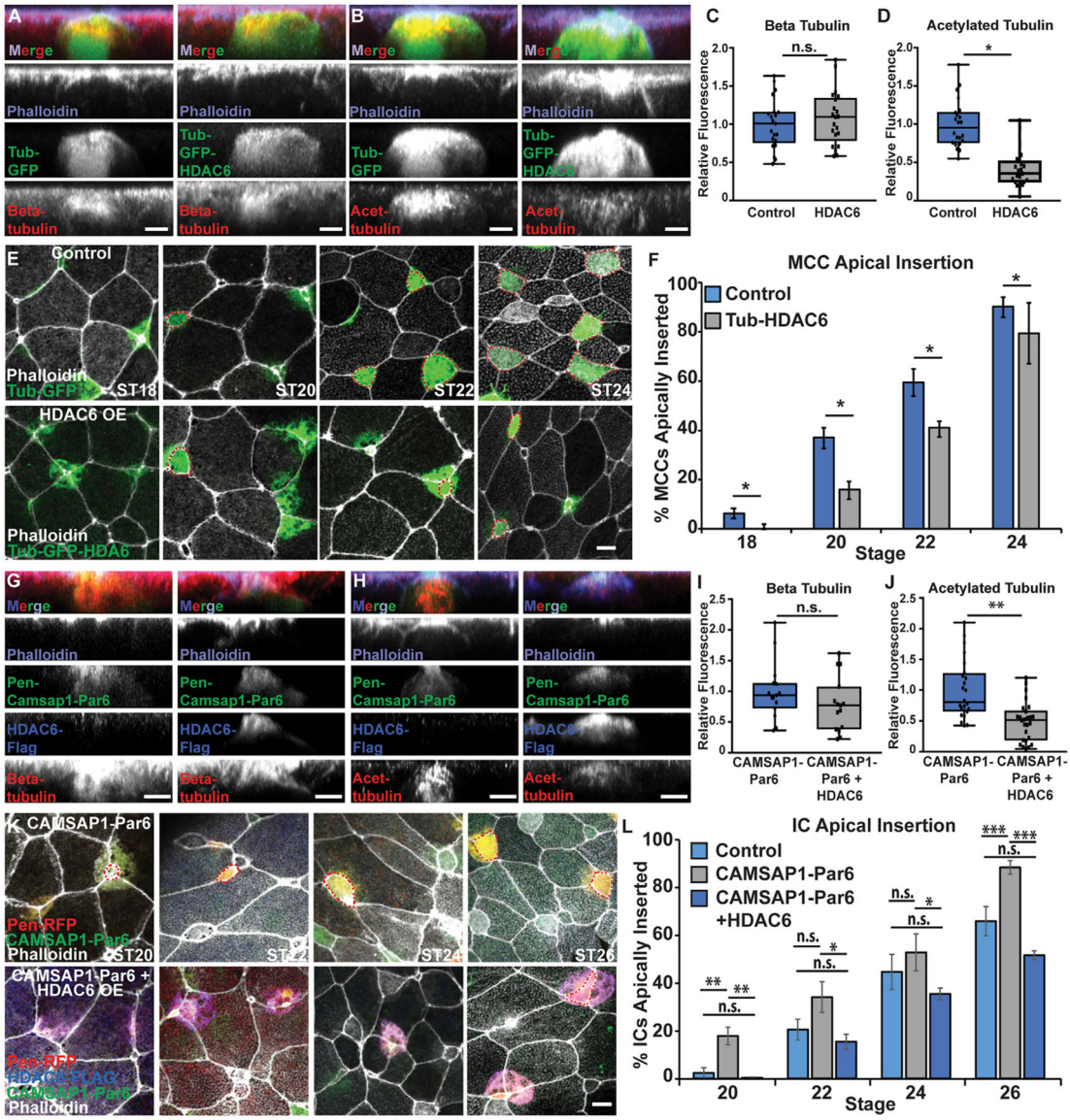

Figure 1. Loss of MT acetylation delays apical insertion

(A and B) Side projections of intercalating control and Tub-GFP-HDAC6 OE MCCs fixed and stained with phalloidin and α-beta tub (A) or α-acetylated (α-acetyl.) tub. (B).

(C and D) Quantification of beta tub (C) and of acetyl. tub (D) in control and HDAC6 OE MCCs. Fluorescence was normalized relative to control (uninjected) MCCs in mosaic embryos for each experiment.

(E) Z-projections of embryos mosaically injected with Tub-GFP or Tub-GFP-HDAC6 DNA and phalloidin to assay apical insertion.

(F) Quantification of the percentage of MCCs apically inserted at each stage.

(G and H) Side projections of intercalating Pen-CAMSAP1-Par6 and Pen-CAMSAP1-Par6 + HDAC6 OE ICs stained with α-FLAG, phalloidin, and α-beta tub (G) or α-acetyl. tub (H).

(I and J) Quantification of beta tub (I) or acetyl. tub (J) in CAMSAP1-Par6 and CAMSAP1-Par6 + HDAC6 OE ICs. Fluorescence was normalized relative to (control) ICs expressing only CAMSAP1-Par6 in mosaic embryos for each experiment.

(K) Z-projections of embryos mosaically injected with Pen-RFP and HDAC6-FLAG DNA and CAMSAP1-Par6 mRNA and stained with α-FLAG and phalloidin to assay apical insertion.

(L) Quantification of the percentage of ICs apically inserted at each stage.

For all bar graphs (F and L), bars represent the average and error bars indicate SD; for all box-and-whisker plots (C, D, I, and J), the box represents 25%–75% range, the line is the median, and the whiskers represent the total change; and *$p < 0.05$, **$p < 0.01$, ***$p < 0.001$.

Analysis includes $n > 80$ cells from at least 6 embryos per condition (C), $n > 60$ cells from at least 5 embryos per condition (D), $n > 175$ cells from at least 9 embryos per condition and ST (F), $n > 15$ cells from at least 5 embryos per condition (I), $n > 25$ cells from at least 7 embryos per condition (J), and $n > 50$ cells from at least 9 embryos per condition/time point (L). Scale bars in (A), (B), (G), and (H) represent 5 μm and in (E) and (K) represent 10 μm.

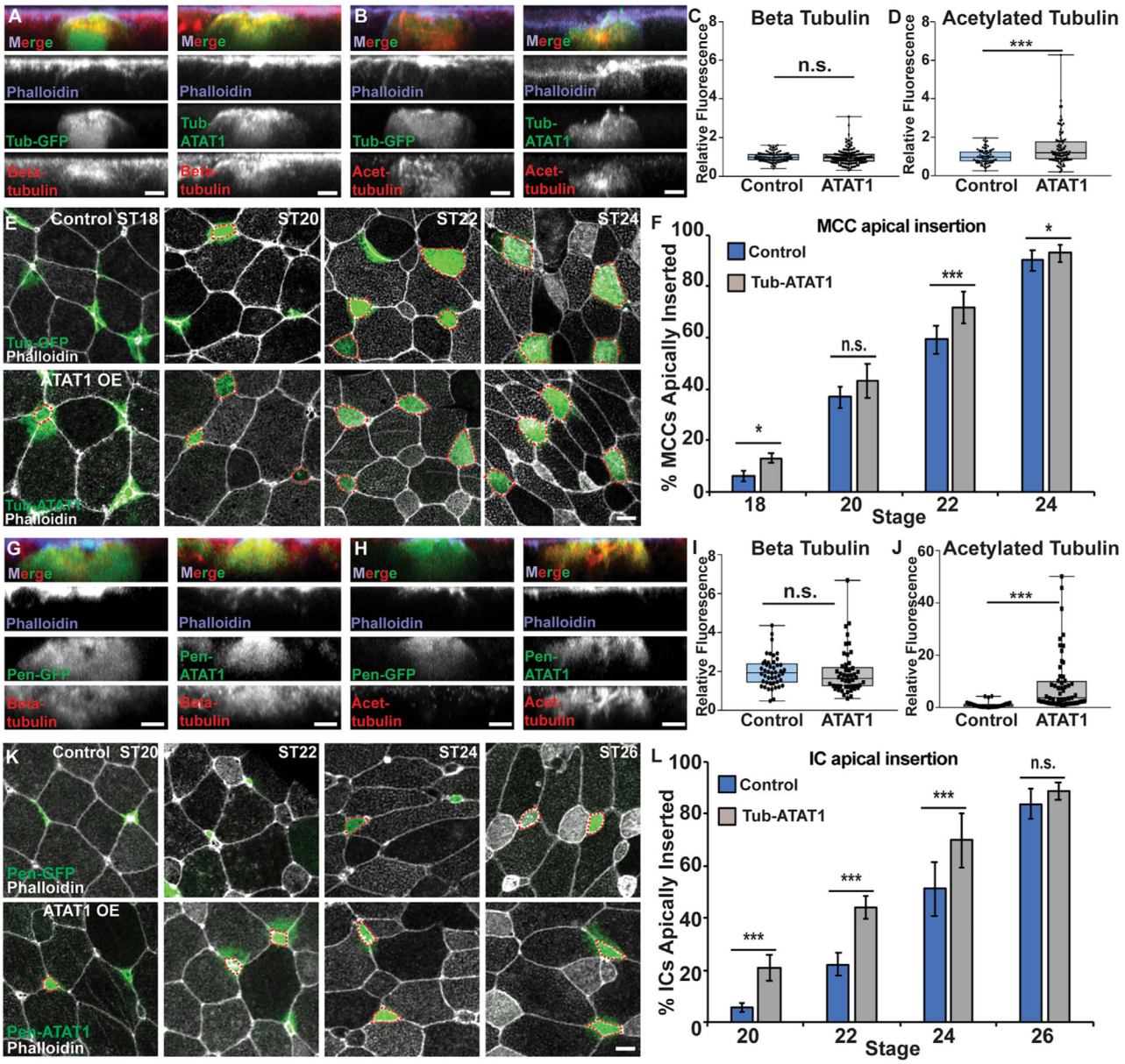

Figure 2. Increased MT acetylation results in precocious apical insertion

(A and B) Side projections of intercalating control and ATAT1 OE MCCs fixed and stained with α-beta tub (A) or α-acetyl. tub (B).

(C and D) Quantification of beta tub (C) and of acetyl. tub (D) in control and ATAT1 OE MCCs. Fluorescence was normalized relative to control (uninjected) MCCs in mosaic embryos for each experiment.

(E) Z-projections displaying progression of MCC apical insertion in control (Tub-GFP) and ATAT1 OE embryos.

(F) Quantification of the percentage of MCCs apically inserted at each stage.

(G and H) Side projections of intercalating control and ATAT1 OE ICs fixed and stained with α-beta tub (G) or α-acetyl. tub (H).

(I and J) Quantification of beta tub (I) and of acetyl. tub. (J) in control and ATAT1 OE ICs. Fluorescence was normalized relative to control (uninjected) ICs in mosaic embryos for each experiment.

(K) Z-projections displaying progression of IC apical insertion in control (Pen-GFP) and Pen-ATAT1 OE embryos.

(L) Quantification of the percentage of ICs apically inserted at each stage.

For all bar graphs (F and L), bars represent the average and error bars indicate SD; for all box-and-whisker plots (C, D, I, and J), the box represents 25%−75% range, the line is the median, and the whiskers represent the total change; and *$p < 0.05$ and ***$p < 0.001$. Analysis includes $n > 100$ cells from at least 6 embryos per condition (C), $n > 80$ cells from at least 5 embryos per condition (D), $n > 200$ cells from at least 9 embryos per condition and ST (F), $n > 15$ cells from at least 3 embryos per condition (I), $n > 50$ cells from at least 5 embryos per condition (J), and $n > 150$ cells from at least 7 embryos per condition and ST (L). Scale bars in (A), (B), (G), and (H) represent 5 μm and in (E) and (L) represent 10 μm.

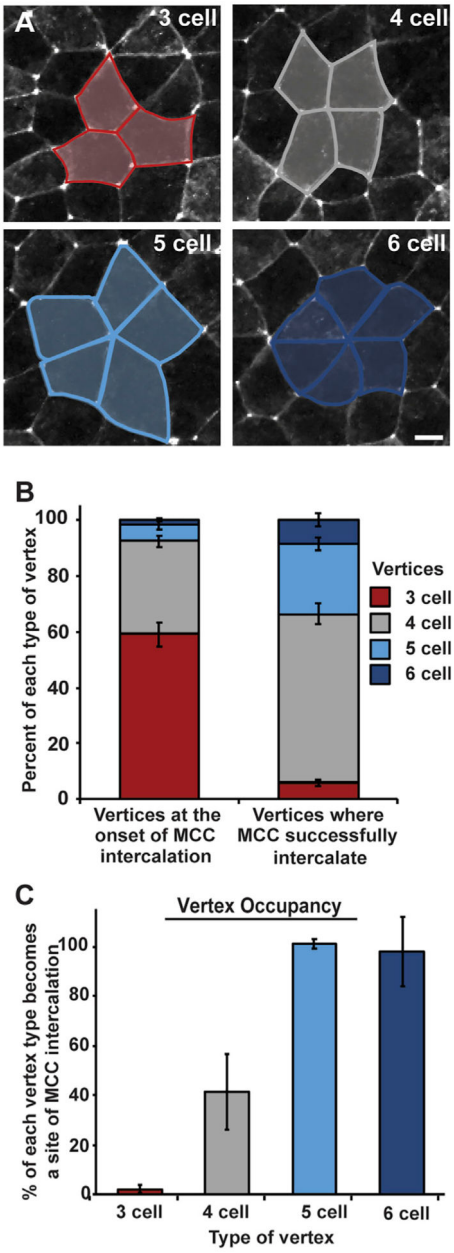

Figure 3. MCCs preferentially intercalate at higher-order vertices

(A) Representative images of 3-, 4-, 5-, and 6-cell vertices between outer epithelial cells expressing GFP-tricellulin (pseudocolored in white); scale bar represents 10 μm. Vertex types are outlined in blue or gray and are representative of graph colors in (B) and (C). (B and C) Analysis of live imaging (e.g., Video S1) quantifying the percentage of each vertex type present in the outer epithelium prior to MCC intercalation (B, left) and sites of successful MCC intercalation (B, right). (C) Percentage of each type of vertex occupied with an MCC by stage 20. Bars represent the mean; error bars indicate SD. Analysis includes n > 1,500 vertices (B, left) and n > 350 MCCs (B, right) from 2 embryos; n > 900 vertices (3 cell), 500 vertices (4 cell), 85 vertices (5 cell), and 30 vertices (6 cell) from 2 embryos (C).

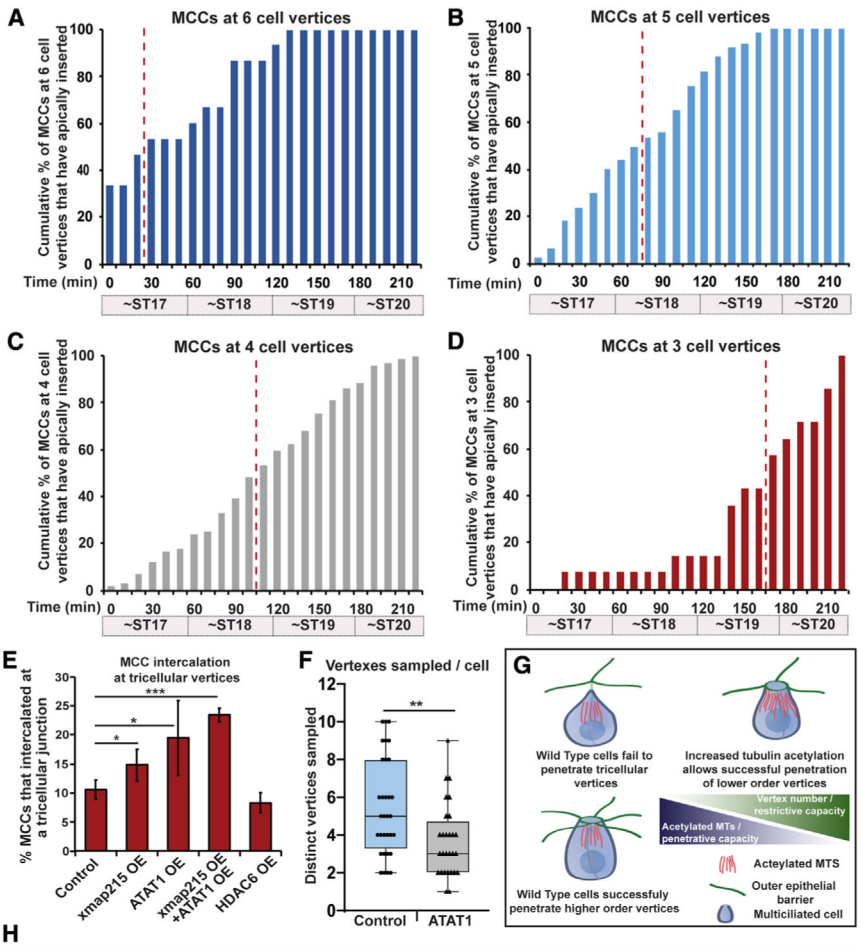

H

k Vertex	Prob. p_k of occurrence	$P_2(k)$	$P_3(k)$	$P_4(k)$	$P_5(k)$	$P_6(k)$	$P_7(k)$	Exp. P(k)	Exp. ATAT1 P(k)
3	60%	36%	21.6%	13%	7.8%	4.7%	2.8%	6%	20%
4	32%	48.6%	56.3%	58.7%	58.1%	56%	53%	58%	52%
5	6%	11.4%	16.2%	20.6%	24.5%	28%	31%	27%	23%
6	2%	4%	5.9%	7.8%	9.6%	11.4%	13.2	9%	5%

Figure 4. Microtubule acetylation alters the penetrative capacity of MCCs

(A–D) Quantification of cumulative percentages of MCCs inserting in the outer epithelium at 6-cell (A), 5-cell (B), 4-cell (C), and 3-cell vertices (D) over time. (A–D) Representative data generated from one time-lapse experiment analyzing intercalation of 214 MCCs. Similar trends were seen in other time-lapse videos. Percentages were calculated by dividing the cumulative number of total MCCs that had breached the outer epithelial layer at each time point by the number of MCCs that inserted at that vertex type. Red dotted line on each bar graph indicates the point at which 50% of the cells that would eventually intercalate at the vertex type had successfully breached the epithelium.

(E) Quantification of the percentage of MCCs that intercalated at tricellular vertices by stage 20. For bar graph in (E), bars represent the mean, error bars indicate SD, and *$p < 0.05$ and ***$p < 0.001$. Analysis includes $n > 350$ cells for each condition from at least 9 embryos (E).

(F) Measured value for q, quantification of the number of vertices sampled prior to apical insertion in control and ATAT1 OE MCCs. Data are from 2 4-h movies of each condition

with an n of 32 cells for control and 28 cells for ATAT1 OE; for box-and-whisker plot, the box represents the 25%−75% range, the line represents the median, and the whiskers represent the total range; and **p < 0.01.

(G) Model of the balance of the restrictive capacity of the epithelium that varies by vertex strength and the penetrative capacity of intercalating cells that varies by the amount of tubulin acetylation.

(H) Probability that an MCC successfully intercalates at a k-vertex, using Equation 1. Experimental data (Exp. P(k) column) is from Figure 3B (right). Distribution of vertex type (Prob. of occurrence column) is from Figure 3B (left). Exp. ATAT1 P(k) represents the observed percentage for each vertex type in MCC OE ATAT1. This table shows the dependence on q of the probability that an MCC successfully intercalates at a k-vertex, using Equation 1.

KEY RESOURCES TABLE

REAGENT or RESOURCE	SOURCE	IDENTIFIER
Antibodies		
anti-acetylated tubulin (mouse)	Sigma-Aldrich	T7451; RRID:AB_609894
anti-beta tubulin E7 (mouse)	Developmental Hybridoma Studies Bank	RRID: AB_2315513
Cy-2-Goat anti-mouse	Abcam	Ab6944; RRID: AB_954987
Cy-3-Goat anti-mouse	MilliporeSigma	AP124CMI; RRID: AB_11213281
Cy-5-Goat anti-mouse	Invitrogen	A10524; RRID: AB_2534033
Chemicals, peptides, and recombinant proteins		
Alexa Fluor™ Plus 405 Phalloidin	Invitrogen	Cat#A30104
Phalloidin, DyLight 650	Invitrogen	Cat# PI21838
Fluorogel	Electron Microscopy Sciences	Cat#1798510
nocodazole	Sigma	Cat#M1404
Critical commercial assays		
mMESSAGE mMACHINE™ SP6 Transcription Kit	Invitrogen	Cat#AM1340
RNeasy Mini Kit	QIAGEN	Cat#74104
Experimental models: Organisms/strains		
Xenopus laevis (female)	Nasco	Cat#LM00535
Xenopus laevis (male)	Nasco	Cat#LM00715MX
Xla.Tg(tuba1a:deup1-eGFP) *NXR*	National *Xenopus* Resource	Cat#NXR_0103
Xla.Tg(tuba1a:MyrPalm-mRFP1) *NXR*	National *Xenopus* Resource	Cat#NXR_0074
Oligonucleotides		
Morpholino: Control MO: 5′-CCTCTTACCTCAGTTACAATTTATA-3′	Gene Tools	N/A
Morpholino: ATAT1 MO: 5′-GTGTACGTCAAACTCAAACTCCATG-3′	Gene Tools	N/A
Primer: ATAT1 for Tub (forward): 5′-GCGAATTCATGGAGTTCCCGTTCGATG-3′	This paper	N/A
Primer: ATAT1 for Tub (reverse): 5′-GCCTCGAGTTAGTATCGACTCTCCTCAGAG-3′	This Paper	N/A
Primer: Xmap215 (forward): 5′-GCATCGATATGGGGGATGACAGCG-3′	This paper	N/A
Primer: Xmap215 (reverse): 5′-GCGAATTCGGCTTTCCGGCTACTTTTG-3′	This paper	N/A
Primer: HDAC6 (forward): 5′-GCGAGCTCATGACCTCAACCGGCCA-3′	This paper	N/A
Primer: HDAC6 (reverse): 5′-GCATCGATTAGTGTGGGTGGGGCATA-3′	This paper	N/A
Primer: ATAT1 for Pen (forward): 5′-GCGGATCCATGGAGTTCCCGTTCGATG-3′	This paper	N/A
Primer: ATAT1 for Pen (reverse): 5′-GCCTCGAGTTAGTATCGACTCTCCTCAGAG-3′	This paper	N/A

REAGENT or RESOURCE	SOURCE	IDENTIFIER
Recombinant DNA		
Tub-GFP in pCS2+ vector	Stubbs et al., 2006	N/A
Tub-RFP in pCS2+ vector	Stubbs et al., 2006	N/A
Pen-GFP in pCS2+ vector	Quigley et al., 2011	N/A
Pen-RFP in pCS2+ vector	Collins et al., 2020a	N/A
GFP-CAMSAP1-Par6 in pCS2+ vector	Collins et al., 2020a	N/A
Tub-GFP-HDAC6 in pCS2+ vector	This paper	modified from Addgene plasmid #13823
Tub-GFP-ATAT1 in pCS2+ vector	This paper	modified from Addgene plasmid #27099
Pen-RFP-ATAT1 in pCS2+vector	This paper	modified from Addgene plasmid #27099
Tub-XMAP215-GFP in pCS2+ vector	This paper	N/A
Software and algorithms		
ImageJ	Schneider et al., 2012	https://imagej.nih.gov/ij/
NIS-Elements	Nikon	https://www.microscope.healthcare.nikon.com/products/software/nis-elements